Wave Inversion Technology, Report No. 4, pages 145-158

Estimating the Global Permeability Tensor using Hydraulically Induced Seismicity — Implementation of a new Algorithm

J. Rindschwentner[1]

keywords: *diffusion, permeability, hydraulic diffusivity, fluid flow*

ABSTRACT

Permeability has a major control on fluid flow since it covers many orders of magnitude and because of its anisotropy. Moreover, estimates of permeability are highly scale dependent. (Shapiro et al., 1997, 1999a) proposed a method to estimate a permeability tensor at reservoir scale using hydraulically induced seismicity. Now, an alternative approach has lead to a new algorithm for estimating the permeability tensor. The algorithm is based on the computation of a pseudo-covariance matrix. With the new algorithm data sets from Soultz-sous-Forêts (France), the KTB site (Germany) and Fenton Hill (USA) were reprocessed and thus the algorithm tested. It proved to produce very reasonable results and facilitates — along with a visualization of the results — the interpretation of possible fluid flow paths. The presented paper is extracted from the author's Master's thesis. The latter was supervised by S. A. Shapiro.

INTRODUCTION

The estimation of hydraulic diffusivity and permeability was introduced in recent years by (Shapiro et al., 1997). At first, they introduced an isotropic estimation which was later extended to the anisotropic case (Shapiro et al., 1999a,b). The method is called 'Seismicity Based Reservoir Characterization' (SBRC). Now, we developed and implemented a new algorithm for estimating the permeability tensor. This was done in the framework of the author's Master thesis. The material presented here is extracted from that thesis.

In the following section we will introduce the main features of the algorithm. Subsequently, we present reprocessed results from Soultz-sous-Forêts (France), the KTB site (Germany) and Fenton Hill (USA). The quality of these results and the potential

[1]**email:** janr@geophysik.fu-berlin.de

of the method for fluid flow interpretations is then discussed in section Discussion of Results.

AN ALTERNATIVE APPROACH FOR A GLOBAL ESTIMATION OF THE PERMEABILITY TENSOR

The algorithm

The new, alternative algorithm is meant to provide a more straightforward estimation of the permeability tensor and shall also yield orientations of the latter which was not possible with the old method (Shapiro et al., 1999a). The following considerations are based on this previously published work. For fundamentals of the method see the contribution of Shapiro et al. in this report.

In the new approach the triggering front can be expressed in the principal coordinate system as follows:

$$\frac{x_1^2}{D_{11}} + \frac{x_2^2}{D_{22}} + \frac{x_3^2}{D_{33}} = 4\pi t. \tag{1}$$

where D_{11}, D_{22} and D_{33} are the principal components of the hydraulic diffusivity.

The transition to a new coordinate system by scaling the original data points in the following way

$$x_{sj} = \frac{x_j}{\sqrt{4\pi t}} \tag{2}$$

yields the triggering front as an equation of an ellipsoid:

$$\frac{x_{s1}^2}{D_{11}} + \frac{x_{s2}^2}{D_{22}} + \frac{x_{s3}^2}{D_{33}} = 1. \tag{3}$$

Hence, all events in the scaled coordinate system – which do not occur before the triggering front – lie within this ellipsoid whose half axes a, b, c are the square roots of D_{11}, D_{22} and D_{33}, respectively. In order to determine the triggering front one needs to find an envelope ellipsoid for the majority of events.

The new space is then divided into a 3-D-grid with cubic cells. We start off with a coarse grid which is refined from run to run. On the next step, the algorithm checks whether a cell is occupied by at least one event. If that is the case, the events in these cells are replaced by the center point of the cell and the cell is selected for further computation. Thus, all selected cells together form a slightly irregular body that resembles an ellipsoid. All void cells are discarded at this point. With the remaining cells we compute a – as we call it – pseudo-covariance matrix. We replace the dividend n of the covariance matrix by the cell volume which is constant for each cell

$$C_{ij} = v(n) \sum_{k=1}^{n} r_{ik} r_{jk} \qquad i, j = 1, 2, 3. \tag{4}$$

The eigenvectors of this matrix yield the orientations of the diffusivity tensor. The magnitudes of the tensor are obtained by equating the irregular body to an ideal ellipsoid. The result relates the eigenvalues e_x, e_y, e_z of the irregular body and the the lengths a, b, c of the half-axes of the ellipsoid:

$$e_x = \frac{1}{5}Va^2, \qquad e_y = \frac{1}{5}Vb^2, \qquad e_z = \frac{1}{5}Vc^2 \tag{5}$$

Further transformations lead to solutions of the D_{ii} expressed by the known eigenvalues e_x, e_y, e_z:

$$D_{11} = a^2 = \frac{5e_x}{\sqrt[5]{2/9\,\pi^2 10^3 e_x e_y e_z}} \tag{6}$$

$$D_{22} = b^2 = \frac{5e_y}{\sqrt[5]{2/9\,\pi^2 10^3 e_x e_y e_z}} \tag{7}$$

$$D_{33} = c^2 = \frac{5e_z}{\sqrt[5]{2/9\,\pi^2 10^3 e_x e_y e_z}}. \tag{8}$$

The orientations of the tensor axes are obtained from the eigenvectors of the pseudo-covariance matrix. They are given – as we will show in the next section – as strike and dip of the vector. The strike is counted clockwise from N and the dip positively downwards.

In order to obtain the permeability tensor we use relations between hydraulic diffusivity and permeability introduced by (Biot, 1962):

$$D_{lm} = \frac{M_c k_{lm}}{\eta} \tag{9}$$

where k_{lm} is the permeability tensor, D_{lm} the hydraulic diffusivity tensor, η is the pore-fluid dynamic viscosity and M_c is the poroelastic modulus. The latter comprises several other parameters. For crystalline rocks with low porosity one can simplify the poroelastic modulus and thus obtains the approximation (Shapiro et al., 1997)

$$M_c = \left(\frac{n}{K_f} + \frac{\alpha}{K}\right)^{-1} \tag{10}$$

where $\alpha = 1 - \frac{K}{K_s}$. The parameters are the bulk modulus of the drained rock K, the bulk modulus of the pore fluid K_f, the bulk modulus of the solid K_s, the porosity n and the coefficient of effective pressure α. Generally, the term n/K_f can not be neglected since $K_f \ll K$ (Shapiro et al., 1997).

RESULTS

Soultz-sous-Forêts

Investigations The injection test in 1993 lasted for about 350 hours and fed about 25,300 m^3 of water into the rock. The injected water induced about 18,000 events of which about 9,300 were localized with sufficient accuracy within 400 hours after the start of injection. The data set was provided by courtesy of SOCOMINE. The events occurred in the depth range from 2,000 m to 3,500 m with the injection source assumedly located at 2,920 m. In fact, the injection was conducted between 2,850 and 3,400 m (Cornet, 2000). However, major fluid loss occurred in the interval from 2,850 to 3,000 m which justifies the assumed point source at 2,920 m (Shapiro et al., 2000). The volume of the seismically active rock approximately comprises 1,5 km^3.

Results The envelope ellipsoid which fits the cloud in the scaled coordinate system best is displayed in figure 1. The ellipsoid is semi-transparent in order to get an idea how well it fits the cloud. As one can see, the ellipsoid extends slightly too far towards S (top view) and apparently does not dip steeply enough (east view). However, generally the fit is quite good for the compact part of the cloud.

The computed orientations of the ellipsoid are as follows. The largest component points in NNW-direction and dips with an angle of about 72° towards N. The medium component points SSE with a dip angle of 18° towards S. The smallest component is about horizontal while pointing ENE (for exact numbers see table 1).

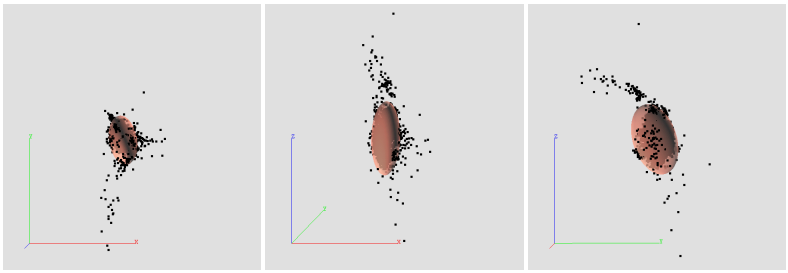

Figure 1: The smaller ellipsoid representing the hydraulic diffusivity tensor shown together with the cloud of events in the scaled coordinate system looking from the top, south and east, respectively.

An alternative estimate yields an envelope ellipsoid that encloses most of the points. However, as figure 2 reveals, vast areas around the compact cloud remain void. The fit of the cloud is obviously influenced by the upward trending events. This is reflected in different orientations compared to the smaller ellipsoid. Now, the maximum component trends N and dips 60°, the medium component S with a dip of 30°

	larger ellipsoid		smaller ellipsoid	
	strike	dip	strike	dip
minimum component	N272°	2°	N259°	0°
medium component	N181°	30°	N169°	18°
maximum component	N5°	60°	N351°	72°

Table 1: Orientations of the principal diffusivities for Soultz.

and the smallest component strikes W and is quasi-horizontal (for exact numbers see table 1).

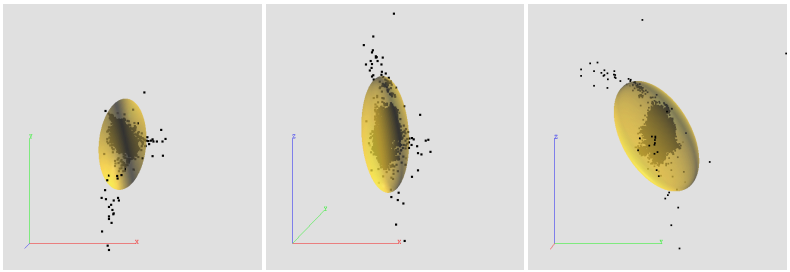

Figure 2: The larger ellipsoid representing the hydraulic diffusivity tensor shown together with the cloud of events in the scaled coordinate system looking from the top, south and east, respectively.

For both ellipsoids, we computed the following hydraulic diffusivity tensors:

$$\begin{pmatrix} 0.7 & 0 & 0 \\ 0 & 1.9 & 0 \\ 0 & 0 & 5.2 \end{pmatrix} \times 10^{-2}\ \mathrm{m}^2/\mathrm{s} \qquad \begin{pmatrix} 1.9 & 0 & 0 \\ 0 & 4.8 & 0 \\ 0 & 0 & 14.2 \end{pmatrix} \times 10^{-2}\ \mathrm{m}^2/\mathrm{s} \tag{11}$$

In order to obtain the permeability tensor we revert to the equations (9) and (10). Log measurements and literature data (Haar et al., 1984) provide the estimates of the necessary parameters (see table 2). The fluid viscosity is that of hot water.

ϕ	η	K	K_f	K_g
0.003	$1.9 * 10^{-4}$ Pa s	49 GPa	2.2 GPa	75 GPa

Table 2: Estimates of poroelastic parameters for Soultz.

That makes $M_c \approx 1.68 \times 10^{11}$ Pa and thus, yields the permeability tensors

$$\begin{pmatrix} 0.8 & 0 & 0 \\ 0 & 2.1 & 0 \\ 0 & 0 & 5.9 \end{pmatrix} \times 10^{-17} m^2 \qquad \begin{pmatrix} 2.2 & 0 & 0 \\ 0 & 5.4 & 0 \\ 0 & 0 & 16.1 \end{pmatrix} \times 10^{-17} m^2 \tag{12}$$

for the smaller ellipsoid and the larger ellipsoid, respectively.

Figure 3 shows the ellipsoid representing the permeability tensor (taken from smaller ellipsoid) in the Cartesian coordinate system together with the cloud of events. This display illustrates well the proportions and orientations of the tensor components. Besides, it makes clear that the ellipsoid does not depend on the shape of the cloud of events.

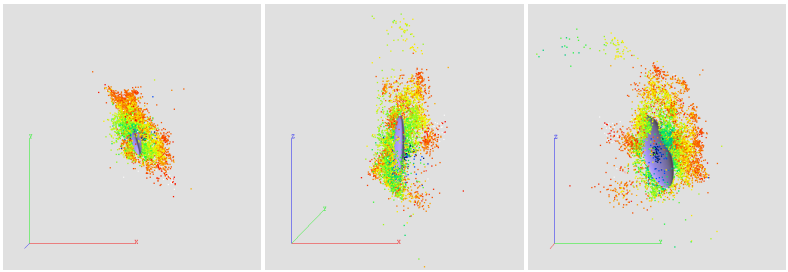

Figure 3: The cloud of events from the 1993 injection experiment at Soultz (France) together with the ellipsoid representing the permeability tensor looking from the top, south and east, respectively.

KTB

Investigations During the experiment 200 m^3 of KBr/KCl brine was injected in the depth interval 9.03–9.1 km over a period of 24 hours. Seventy-three short-period seismometers at the surface and one 3-component downhole seismometer installed at 4 km depth recorded more than 400 microearthquakes in 60 hours. Ninety-four of these earthquakes could be localized with respect to 'master' events with a relative location accuracy of several 10's of meters (Zoback and Harjes, 1997). Magnitudes were larger than -1.5 with a maximum of 1.2. They represent the data we used with courtesy of Hans-Peter Harjes[2]. The seismically active rock comprises a volume of approximately 0.35 km^3.

Results In order to be able to apply our method we had to mirror the cloud at the injection point. However, the result obtained is only valid for the volume above the injection point since seismic activity was only found there. Moreover, the results obtained contain some uncertainty. This is taken into account and we obtain the following hydraulic diffusivity tensor

$$\begin{pmatrix} 4.0\ldots9.6 & 0 & 0 \\ 0 & 12.0\ldots21.5 & 0 \\ 0 & 0 & 96.0\ldots173.6 \end{pmatrix} \times 10^{-2}\ \mathrm{m}^2/\mathrm{s}. \qquad (13)$$

[2]Department of Geophysics, Ruhr University Bochum, Bochum, Germany

Thus, the range of values obtained is considerable with the upper bound being almost twice as large as the lower bound. The orientations only differ slightly.

The envelope ellipsoid computed encloses most of the events in the scaled coordinate system (figure 4). The fit is reasonable considering the low density and small number of events. We will return to this in the discussion. The link to permeability

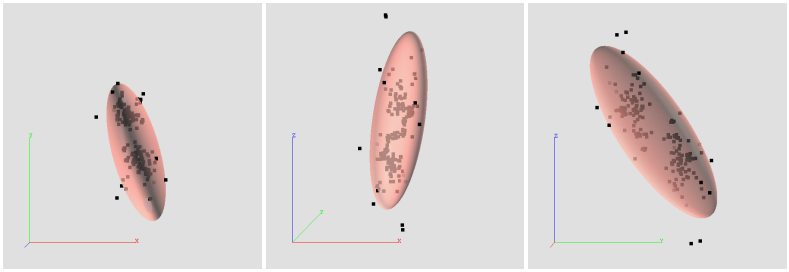

Figure 4: The ellipsoid representing the hydraulic diffusivity tensor at the second kink shown together with the cloud of events in the scaled coordinate system looking from the top, south and east, respectively

is given by the equations (9) and (10). Log measurements and literature data (Bram and Draxler, 1995; Emmermann et al., 1995) provide the estimates of the necessary parameters. (Shapiro et al., 1997) assumed properties of water for the fluid and thus obtained the following parameters

ϕ	η	K	K_f	K_g
0.003	$1.0 * 10^{-4}$ Pa s	50 GPa	2.3 GPa	70 GPa

Table 3: Estimates of poroelastic parameters for the KTB.

Hence, $M_c \approx 2 \times 10^{11}$ Pa and thus, yields the following permeability tensors

$$\begin{pmatrix} 0.2 \ldots 0.48 & 0 & 0 \\ 0 & 0.6 \ldots 1.08 & 0 \\ 0 & 0 & 4.8 \ldots 8.68 \end{pmatrix} \times 10^{-16}\ \mathrm{m}^2. \qquad (14)$$

Figure 5 illustrates the large difference between the largest and the smallest component of the permeability tensor. The ellipsoid representing the permeability tensor is shown in the Cartesian coordinate system together with the cloud of events. This display makes clear that the ellipsoid does not depend on the shape of the cloud of events.

Fenton Hill

Investigations The data set of microearthquakes we work with was recorded during the massive hydraulic fracture experiment (MHF) in December 1983. It was provided

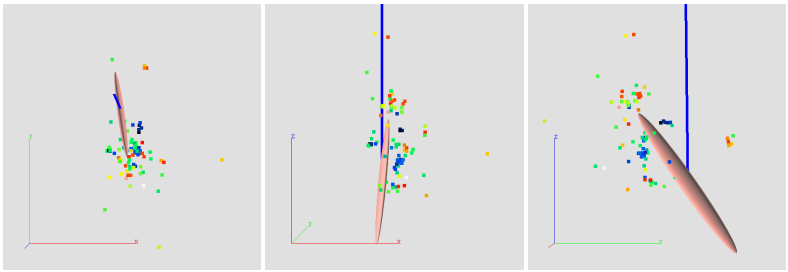

Figure 5: The cloud of events from the 1993 injection experiment at the KTB site together with the ellipsoid representing the permeability tensor looking from the top, south and east, respectively.

by courtesy of Micheal Fehler[3]. For 61 hours, 21,600 m^3 of water was injected at a depth of about 3,460 m (House, 1987). The injection occurred through a 20 m open-hole interval. No events were recorded in the first 5 hours. In the time span from 30 to 40 hours after the injection only three stations were in operation and therefore, no data was analyzed (Fehler et al., 1998).

Registration of seismicity occurred with four geophones. The instruments were deployed in four different boreholes, i.e. in EE-1 at 2,850 m, in EE-3 at 3,300 m, in GT-2B at 2,440 m, in GT-1 at 820 m, in PC-1 at 570 m depth. The stations EE-1, EE-3 and GT-1 were located within the basement rocks and station PC-1 within a cavernous limestone formation, approximately 150 to 200 m above the basement (Block et al., 1994). The accuracy of the earthquake locations was better than 100 m. The relative location uncertainty was even brought down to 20 to 30 m (House, 1987).

Results The smallest ellipsoid only contains the more compact inner cloud of events (figure 6). The fit looks very good in east view whereas in top view the NE part appears overpronounced which is confirmed by the display in south view. As a comparison, figure 7 shows how the larger, computed ellipsoid encloses almost all points. Thereby, most of the space within the ellipsoid is not filled by events. The size and the shape is due to the outliers making the ellipsoid rounder and more spherical. All ellipsoids have significantly different orientations. The second largest ellipsoid's maximum half-axis strikes SW and dips 60°. The other two half-axes reveal a strike of ESE and NNE and a dip of 12° and 27°, respectively. The smaller ellipsoid has orientations of NW and ENE as well as dips of 57° and 4° for the smaller half-axes, respectively. The largest half-axis runs SSE and dips 33° (for exact values see table 4). The cloud of events in the scaled coordinate system forms a rather compact inner cloud. Around it one finds almost uniformly distributed events (outliers) with no preferential direction. They are responsible for the estimates of the two larger ellipsoids.

[3]Geological Engineering Group, Los Alamos National Laboratory, Los Alamos, NM 87545, USA

	largest ellipsoid		medium ellipsoid		smallest ellipsoid	
	strike	dip	strike	dip	strike	dip
minimum component	N350°	15°	N12°	27°	N69°	4°
medium component	N87°	25°	N109°	12°	N332°	57°
maximum component	N233°	61°	N220°	60°	N161°	33°

Table 4: Orientations of the principal diffusivities for Fenton Hill.

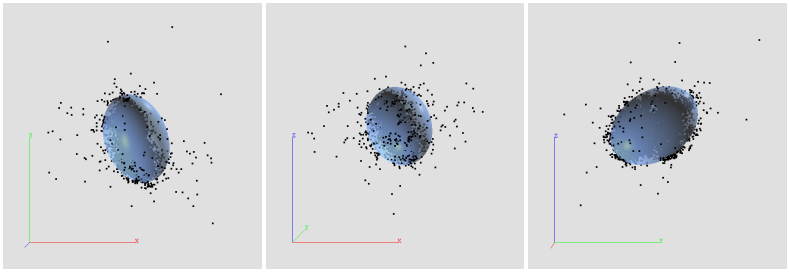

Figure 6: The ellipsoid representing the hydraulic diffusivity tensor shown together with the cloud of events in the scaled coordinate system looking from the top, south and east, respectively.

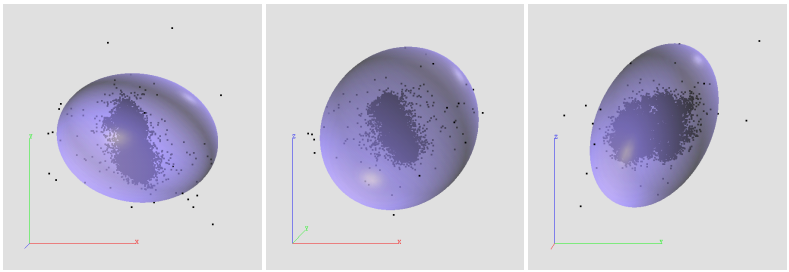

Figure 7: The ellipsoid representing the hydraulic diffusivity tensor shown together with the cloud of events in the scaled coordinate system looking from the top, south and east, respectively.

Both ellipsoids correspond to the following estimates of the hydraulic diffusivity tensor

$$\begin{pmatrix} 5.9 & 0 & 0 \\ 0 & 7.2 & 0 \\ 0 & 0 & 14.2 \end{pmatrix} \times 10^{-2}\,\mathrm{m}^2/\mathrm{s} \qquad \begin{pmatrix} 17.2 & 0 & 0 \\ 0 & 34.8 & 0 \\ 0 & 0 & 40.9 \end{pmatrix} \times 10^{-2}\,\mathrm{m}^2/\mathrm{s}. \quad (15)$$

Again, we revert to the equations (9) and (10) for computing the permeability tensor. Values for the needed poroelastic parameters are gathered from literature (after (Shapiro et al., 1999b)). The fluid viscosity η, i.e., is that of hot water. That makes

ϕ	η	K	K_f	K_g
0.003	$1.9 * 10^{-4}$ Pa s	49 GPa	2.2 GPa	75 GPa

Table 5: Estimates of poroelastic parameters for Fenton Hill.

$M_c \approx 1.68 \times 10^{11}$ Pa and thus, yields the permeability tensors

$$\begin{pmatrix} 0.67 & 0 & 0 \\ 0 & 0.81 & 0 \\ 0 & 0 & 1.61 \end{pmatrix} \times 10^{-16}\text{m}^2 \qquad \begin{pmatrix} 1.95 & 0 & 0 \\ 0 & 3.94 & 0 \\ 0 & 0 & 4.63 \end{pmatrix} \times 10^{-16}\text{m}^2 \tag{16}$$

for the smaller ellipsoid and the larger ellipsoid, respectively.

In Figure 8 one can see that the difference between the largest and the smallest component of the permeability tensor is not nearly as distinct as at the KTB site. The ellipsoid representing the permeability tensor (obtained form the smaller ellipsoid) is shown in the Cartesian coordinate system together with the cloud of events. This display makes clear that the ellipsoid does not depend on the shape of the cloud of events.

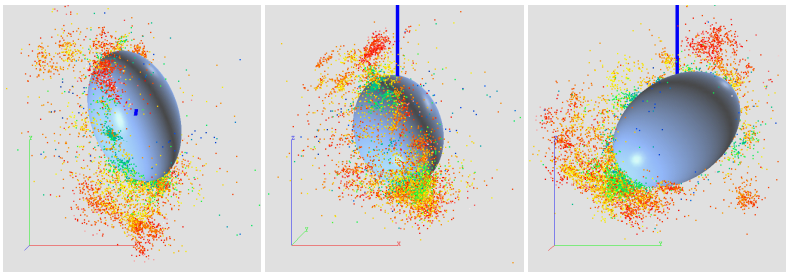

Figure 8: The cloud of events from the 1993 injection experiment at the KTB site together with the ellipsoid representing the permeability tensor looking from the top, south and east, respectively.

DISCUSSION OF RESULTS

The results from the different sites reveal some similarities. Most important for us is the fact that all results agree well with independently determined permeability values at comparable scales. Thus, the magnitudes obtained can be considered highly reasonable. Results previously obtained by (Shapiro et al., 1998, 1999a,b) with the old method are confirmed by computations with the new algorithm. Only at Fenton Hill, the new minimum component is slightly smaller due to reason discussed below. Moreover, the orientations of the tensors coincide with stress and fracture orientations

found at the respective sites except at the Fenton Hill site. Here, the information on stress and fracture orientations do not suffice to be able to compare them to our results. However, the notion of the 'comple x fracture system' (House, 1987) can be interpreted as a confirmation of our round ellipsoid where the difference between the maximum and the minimum component is merely 3 to 1. That means there is only a weakly pronounced preferential direction of fluid flow. This situation is very likely in a complex fracture system. At the other two sites fluid flow will be most distinct in direction of the dominating fracture system.

The figures 1, 4 and 6 of the envelope ellipsoids together with the cloud of events in the scaled coordinate system allow to judge the quality of the fit of the ellipsoids to the clouds. Especially at Soultz (figure 1), the fit is very good. Only in east view one can see a certain misfit that leads to a smaller dip angle for the maximum component. So, instead of 74° the dip is rather 80° or more. At Fenton Hill (figure 6) the north view shows that the magnitude of the smallest component striking roughly EW was a little (factor 2 to 3) overestimated. Also slightly overestimated might be the entire ellipsoid at the KTB site (figure 4) although – due to the few events – this is rather speculative. The proportions of the three components, however, look right. Secondly, we observe that this way of presenting the results gives some impression of irregularities. Figure 6 from Fenton Hill, e.g., reveals differences in the extension of the cloud southward and northward from the center and also eastward and westward. Once more, heterogeneities might be the reason for that. The same consideration applies to figure 1 from Soultz were upward and downward extension differ a little. Generally, we conclude that the plain numbers of the tensors and the orientations represent a reasonable result. However, considering the scaled cloud together with the semi-transparent ellipsoid adds some qualitative information which might improve the interpretation.

Another illustration facilitates the understanding of the results as well as of the method. Figures 3, 5 and 8 visualize the permeability tensor. The ellipsoid corresponding to the latter is plotted in the Cartesian coordinate system together with the cloud of events. Thus, one obtains a good impression of the proportions of the tensor components as well as of their orientations. This simplifies the interpretation of possible fluid paths. Moreover, the display shows that the shape of the cloud in the Cartesian system does not coincide with the tensor orientation because it is not relevant for determining the tensor. The estimation of the tensor is exclusively dependent on the shape of the cloud in the scaled coordinate system (see also (Shapiro et al., submitted 2000)).

CONCLUSION

We have implemented a new, alternative algorithm to estimate the permeability tensor. Running time is short – between 10 and 20 minutes – and the whole procedure is rather

straightforward. The new approach was tested on various data sets with different characteristics and proved to produce very reasonable results. Along with the visualization of the tensors as ellipsoids in goCad the method represents a quite powerful tool for estimating fluid flow paths and transport capacities. Thus, it complements the SBRC method very well.

REFERENCES

Biot, M. A., 1962, Mechanics of deformation and acoustic propagation in porous media: Journal of Applied Physics, **33**, 1482–1498.

Block, L. V., Cheng, C. H., Fehler, M. C., and Phillips, W. S., 1994, Seismic imaging using microearthquakes induced by hydraullic fracturing: Geophysics, **59**, 102–112.

Bram, K., and Draxler, J. K., 1995, Basic research and borehole geophysics (final report): KTB Report 94-I.

Cornet, F. H., 2000, Comment on "Large-scale in situ permeability tensor of rocks from induced microseismicity" by S. A. Shapiro, P. Audigane and J.-J. Royer: Geophysical Journal International, **140**, 465–469.

Emmermann, R., Althaus, E., Giese, P., and Stöckhert, B., 1995, Results of geosientific investigation in the KTB field laboratory (Final report): KTB Report 95-2, KTB Hauptbohrung.

Fehler, M., House, L., Phillips, W. S., and Potter, R., 1998, A method to allow temporal variation of velocity in travel-time tomography using microearthquakes induced during hydraulic fracturing: Tectonophysics, **289**, 189–201.

Haar, L., Gallagher, J. S., and Kell, G. S., 1984, NBS/NRC Steam Tables: Thermodynamics and Transport Properties and Computer Programs for Vapor and Liquid States of Water in SI units: Hemispher, New York, 1st edn edition.

House, L., 1987, Locating microearthquakes induced by hydraulic fracturing in crystalline rocks: Geophysical Research Letters, **14**, 919–921.

Rindschwentner, J., November 2000, Estimating the Global Permeability Tensor using Hydraulically Induced Microseismicity – Implementation of a new Algorithm: Master's thesis, Free University of Berlin, Berlin.

Shapiro, S. A., Huenges, E., and Borm, G., 1997, Estimating the crust permeability from fluid-injection-induced seismic emission at the KTB site: Geophysical Journal International, **131**, F15–F18.

Shapiro, S. A., Royer, J.-J., and Audigane, P., 1998, Estimating the permeability from fluid-injection induced seismicity Estimating the permeability from fluid-injection induced seismicity, Balkema, Poromechanics – A Tribute to Maurice A. Biot, 301–305.

Shapiro, S. A., Audigane, P., and Royer, J. J., 1999a, Large-scale in situ permeability tensor of rocks from induced seismicity: Geophysical Journal International, **137**, 207–213.

Shapiro, S. A., Audigane, P., Royer, J.-J., and Fehler, M., 1999b, An inversion for the permeability tensor by using seismic emission: An inversion for the permeability tensor by using seismic emission:, SEG, SEG-Annual Meeting Abstracts, 1,783–1,786.

Shapiro, S. A., Audigane, P., and Royer, J.-J., 2000, Reply to comment by F. H. Cornet on `Large-scale in situ permeability tensor of rocks from induced microseismicity': Geophysical Journal International, **140**, 470–473.

Shapiro, S. A., Rothert., E., Rath, V., and Rindschwentner, J., submitted 2000, Characterization of fluid transport properties of reservoirs using induced microseismicity: Geophysics.

Zoback, M. D., and Harjes, H.-P., 1997, Injection-induced earthquakes and crustal stress at 9 km depth at the KTB deep drilling site, Germany: Journal of Geophysical Research, **102**, 18,477–18,491.

PUBLICATIONS

A detailed presentation of the computation of the hydraulic diffusivities and the features of the algorithm as well as elaborated results were published by (Rindschwentner, 2000).